https://doi.org/10.5194/egusphere-2026-3264
Preprint. Discussion started: 16 June 2026

Localized incipient dehydration in antigorite serpentinite during deformation experiments at subduction zone conditions

Danielle S. Souza[1], Daniel Frost[1], Florian Heidelbach[1], Marcel Thielmann[2]

[1]Bayerisches Geoinstitute, Bayreuth Universität , Bayreuth , 95447, Germany
[2] Institut für Geowissenschaften, Universität Bonn, Bonn, 53115, Germany

Correspondence to: Danielle S. Souza (danielle.silva-souza@uni-bayreuth.de)

Abstract. Intermediate-depth earthquakes are commonly linked to slab dehydration, with dehydration embrittlement of antigorite proposed as a dominant mechanism of brittle failure. However, experimental results increasingly suggest that classical dehydration embrittlement alone may not fully explain intermediate-depth seismicity. Recent work shows that localized incipient dehydration can occur in antigorite due to chemical heterogeneities and stress, forming olivine-rich veins that are also observed in natural serpentinites. These sites may represent regions of strain localization where failure can develop as deformation proceeds. To determine whether deformation promotes localized incipient dehydration relative to hydrostatic conditions, and whether this process contributes to antigorite brittle failure, we investigated the incipient dehydration of antigorite using a six-ram multi-anvil apparatus under both hydrostatic and deviatoric stress conditions. Experiments were conducted across the antigorite stability field at pressures of 3 GPa, temperatures of 530–712 °C, and strain rates of 10-4- 10-5 s-1. Localized incipient dehydration occurs within the antigorite stability field during both static and deformation experiments. Nanocrystalline clusters, veins, and networks containing olivine and pyroxene are observed in all experiments. Localized dehydration is enhanced during deformation experiments, leading to the development of distinct microstructures relative to static conditions. However, this process promotes failure only at fast strain rates (~10^{-4} s^{-1}), suggesting that incipient or even complete dehydration alone is insufficient to cause embrittlement at laboratory conditions.

1 Introduction

Dehydration within subducting lithospheric slabs is considered to occur between ~50 and 300 km depth (Poli and Schmidt, 2002) and has been associated with intermediate-depth earthquakes that occur over a similar depth interval (Zhan, 2020). Dehydration embrittlement is a leading explanation for brittle failure at these depths (Frohlich, 2009; Jung et al., 2004; Zhan, 2020). In this mechanism, shear fracturing develops through the linkage of tensile microcracks aligned perpendicular to the tensile stress and kept open by elevated pore pressure generated during dehydration (Frohlich, 2009; Houston, 2015). This reduces the effective normal stress required for brittle failure (Houston, 2015). This classical dehydration embrittlement mechanism requires a net positive dehydration volume change and sufficiently rapid dehydration such that pore pressure buildup is not relaxed by plastic flow (Gasc et al., 2011).

Dehydration embrittlement of antigorite has been studied extensively because it is stable at pressures and temperatures consistent with intermediate-depth seismicity. Most experiments have been conducted in Paterson and Griggs apparatuses at

https://doi.org/10.5194/egusphere-2026-3264
Preprint. Discussion started: 16 June 2026

pressures up to ~1.5 GPa, whereas a smaller number of studies have used deformation multi-anvil (D-DIA) systems to reach ~6 GPa under hydrostatic or deviatoric stress conditions (Chollet et al., 2011; Dobson et al., 2002; Eberhard et al., 2025; Ferrand et al., 2017; Gasc et al., 2011, 2017; Jung et al., 2004; Okazaki and Hirth, 2016; Raleigh and Paterson, 1965). Despite extensive experimental support for the dehydration embrittlement hypothesis (Dobson et al., 2002; French et al., 2019; Raleigh and Paterson, 1965), several studies argue that dehydration embrittlement alone cannot fully explain intermediate-depth seismicity (Ferrand et al., 2017; Gasc et al., 2011, 2017; Jung et al., 2004; Proctor et al., 2015). These studies show that acoustic emissions (AE) generated during antigorite dehydration under deviatoric stress are weaker than expected for large seismic events (Gasc et al., 2017), and that AE are produced even when dehydration occurs with a net negative volume change (Jung et al., 2004). Alternative mechanisms have therefore been proposed, such as dehydration-driven stress transfer (Ferrand et al., 2017). In this DDST mechanism, dynamic failure occurs in strong olivine surrounding weaker dehydrating antigorite. Another model proposes that the separation of dehydration fluids and solid reaction products promotes local positive volume changes and Mode I (tensile opening) crack propagation at pressures relevant to intermediate seismicity (Jung et al., 2004).

Recent experimental and modelling studies have emphasized that antigorite dehydration is influenced not just by temperature and pressure but also by chemical heterogeneities and deviatoric stress, resulting in localized bands of dehydration under pressure and temperature conditions that would otherwise lie within the antigorite stability field (Eberhard et al., 2025; French et al., 2019; Huber et al., 2024; Plümper et al., 2017; Schmalholz et al., 2023). This localized dehydration produces fine bands of olivine in experimental samples and olivine vein networks in natural incipiently dehydrated serpentine (Eberhard et al., 2025; Muñoz-Montecinos et al., 2024; Plümper et al., 2017). However, the mechanism behind the localized dehydration remains uncertain. Some authors propose that olivine veins may form through a passive process controlled by chemical heterogeneity, in which porosity and olivine nucleation are localized due to different effective temperatures of dehydration (Huber et al., 2024; Plümper et al., 2017). On the other hand, it has been argued that the formation of olivine veins is a dynamic process influenced by plastic deformation that promotes locally accelerated reaction kinetics (Eberhard et al., 2025).

These localized dehydration fronts are potential sites of strain concentration that might lead to brittle failure. In this study we aim to investigate the role of deviatoric stress on the nucleation and spatial distribution of antigorite dehydration products within the antigorite stability field (~530°C ; 3 GPa). We conduct experiments under hydrostatic and deviatoric stress conditions in natural cores of antigorite with a six ram multi-anvil apparatus.

2 Materials and Methods

2.1 Starting Material

The starting material is a natural serpentine rock, primarily consisting of a fine-grained serpentine matrix (~5 µm) containing lenses of larger serpentine grains (>> 5 µm), diopside porphyroblasts and minor magnetite and pentlandite. The average

https://doi.org/10.5194/egusphere-2026-3264
Preprint. Discussion started: 16 June 2026

composition of antigorite is 23.23 wt.% Mg, 18.75 wt.% Si and 2.92 wt.% Fe. It contains a minor average amount of aluminium (0.77 wt.%), which is heterogeneously distributed between antigorite grains with a maximum value of 1.35 wt.% (see Figure S1 and Table S1). In the matrix, there are regions (Figure 1d) where aluminium concentration can reach an average of 6.97 wt.% and a maximum of 10.82 wt.%. These Al-rich regions are often localized near diopside or magnetite grains, with an anhedral shape and an average area of ~200 µm2. Raman spectroscopy confirms that the serpentine is antigorite, with main Raman peaks at 678.3 cm^{-1}, 519.7 cm^{-1} and 369.6 cm^{-1} (Figure S2).

Foliation is not observable at hand scale in the sample, however some light green layers containing aligned diopside porphyroblasts are observed to alternate with dark green layers dominated by antigorite. Cores with a diameter of 2 mm and a height of 3 mm were drilled parallel to these macroscopic layers, within the dark green regions to avoid diopside grains. Nevertheless, some drilled samples still contained unavoidable heterogeneities. Cores that comprised at least 90% antigorite were chosen for the experiments.

In thin section, serpentine is colourless and presents low relief. Under cross-polarizers serpentine shows maximum pale-yellow interference colours. Extinction is parallel to the fibre length. The fine matrix has an interlocking microstructure containing lenses of long fibres. Electron microscopy images of the fine matrix reveal that the serpentine has a radial growth habit (Figure 1).

Qualitative Electron Backscattered Diffraction (EBSD) analysis of serpentine orientation shows that it has a weak crystallographic preferred orientation (CPO), with an M-index = 0.09. From the pole figures it is possible to observe that the basal planes of antigorite (001) have maxima oriented at an oblique angle (SW-NE) relative to the drilling direction. Additionally, the poles of the basal planes are dispersed along a great circle slightly inclined to the XY plane, reflecting the radial growth microstructure (Figure S3).

https://doi.org/10.5194/egusphere-2026-3264
Preprint. Discussion started: 16 June 2026

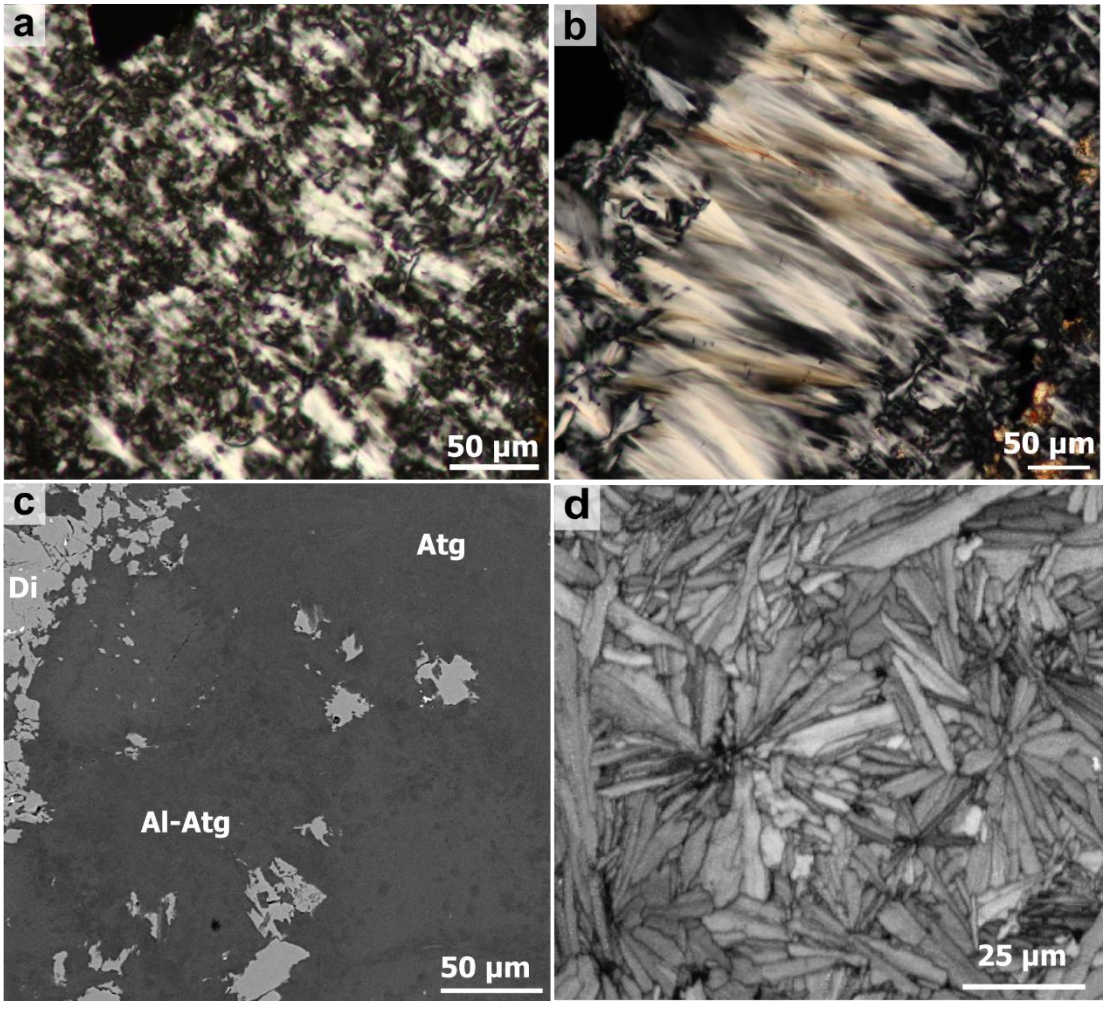

Figure 1- Microstructures of antigorite in the starting material. (a–b) Interlocked and fibrous microstructure in the fine matrix and lenses of antigorite under polarized light. (c) Backscattered electron image of the antigorite matrix (Atg) showing Al-rich antigorite (Al-Atg) regions near diopside grains (Di).(d) Band contrast image from EBSD analysis showing radial growth of antigorite crystals in the matrix.

2.2 Experimental set up

The experiments were performed using a six-ram multi-anvil press located at the Bayerisches Geoinstitute (BGI). This large-volume press uses six independently adjustable anvils to compress a cubic assembly, allowing for precise control over its geometry or deliberate deformation under significant loads (Manthilake et al., 2012).

Five experiments were performed, three at static conditions and two under deviatoric stress conditions. The samples were first compressed at room temperature up to 3 GPa, then brought to the target temperature and annealed for at least 30 minutes

https://doi.org/10.5194/egusphere-2026-3264
Preprint. Discussion started: 16 June 2026

before the deformation (See Table 1). After completion of the annealing or deformation cycle, samples were quenched by manually decreasing the power to zero over an interval of approximately 5 minutes to avoid formation of contraction cracks. The experiment was then decompressed over 1000 minutes to avoid decompression fractures.

Experiments were conducted using a cubic Cr2O3-doped MgO assembly, of 12 mm edge length containing a stepped graphite furnace. This assembly was compressed using square faceted WC anvils of 9 mm edge length. The antigorite cores were wrapped in 25 µm thick platinum foil, folded at both ends, that were sealed against fluid loss once under pressure. For hydrostatic experiments, the capsule was placed in an MgO sleeve and temperature was measured using a type D thermocouple inserted within a 4-bore alumina thermocouple sleeve. An MgO disk protected the capsule from the thermocouple and the plug below the sample consisted of both crushable and solid alumina (Figure 2). Pressure was estimated based on a calibration using the Bi II-III transition.

Static dehydration experiments were conducted at temperatures within the stability field of antigorite (M910, M947) and above it (M909). Power versus temperature curves were generated from experiments M909 and M910. Experiment M909 was annealed above the antigorite stability field for 60 minutes, while M910 and M947 were annealed inside the stability field for 60 and 1260 minutes, respectively, to test the kinetics of the incipient dehydration reaction (see Table 1).

Deformation experiments were conducted in pure shear geometry by advancing one pair of rams (r3-r4) while simultaneously withdrawing perpendicular rams (r5-r6 and keeping the third pair of rams (r1-r2) stationary imposing a pure shear deformation on the sample under constant volume conditions. Compression (rams r3-r4) was along the sample cylinder axis and extension (rams r5-r6) perpendicular to it. Confining pressure (rams r1-r2) was kept constant during the deformation cycle, which lasted 30 to 1260 minutes. The ideal strain rate (Table 1) was calculated from the expected shortening of the sample capsule over the duration of the deformation cycle. The measured strain rate was obtained by displacement rate of anvils r3-r4, measured using Heidenhain displacement sensors with a sensitivity of 0.1 µm. The displacement rate was then normalized to the initial sample length to determine the strain rate.

The deformation experiments (M923, M928) were performed at ~530 °C at different strain rates. These experiments were conducted without thermocouples, following the power versus temperature curve determined from experiment M910. In these experiments, the thermocouple, MgO, and alumina discs were replaced by hard alumina pistons on both sides of the capsule (figure 2). The absence of crushable alumina in this assembly may have induced some deformation during the compression stage before the deformation cycle. Experimental conditions are shown in table 1.

Recovered samples from deformation experiments were cut in half parallel to the plane containing the compression and extension directions, whereas samples from static experiments were cut in half parallel to the heating direction. One half of each sample was mounted in epoxy resin and polished using standard metallographic methods. Final chemical-mechanical polishing was performed using colloidal silica in a semi-automatic rotary polisher for 2h per sample.

https://doi.org/10.5194/egusphere-2026-3264
Preprint. Discussion started: 16 June 2026

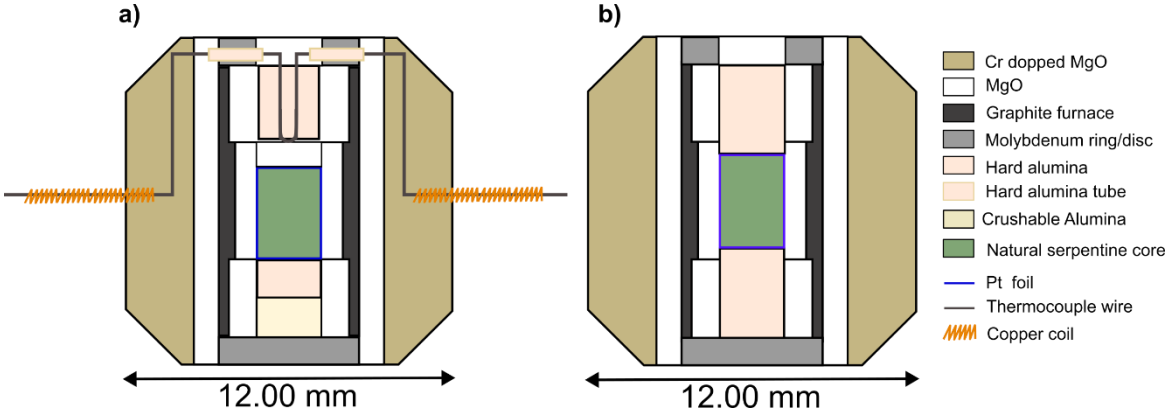

Figure 2 - Ceramic assembly used in the static (a) and pure shear deformation (b) experiments.

Table 1 Experimental conditions. Temperatures marked with * are estimated from the power vs. temperature curve determined in M909. L0 and Li are initial and final capsule length respectively. Li was measured from SEM images of polished sections of recovered samples.

Exp.	T (°C)	Oil P (bar)	Anneal dur. (min)	Deform. dur. (min)	L_0 (mm)	L_i (mm)	Ideal strain (%)	Meas. strain (%)	Ideal strain rate (s^{-1})	Meas. strain rate (s^{-1})	R3-4 displacement rate (s^{-1})
M909	712	52	120	NA	3.1	2.9	NA	NA	NA	NA	NA
M910	560	52	60	NA	3	2.8	NA	NA	NA	NA	NA
M923	534*	52	50	1260	3.7	2.2	30	42	3.97E–06	5.56E–06	1.28E–06
M928	534*	52	30	30	3.8	2.09	20	46	1.11E–04	2.56E–04	1.04E–04
M947	529	52	1260	NA	3.2	2.9	NA	NA	NA	NA	NA

2.3 Analytical methods

2.3.1 Micro-Raman analysis

Micro-Raman analysis was performed on the starting material to characterize the serpentine minerals. Analyses were carried out with a Horiba LabRam spectrometer equipped with a HeNe laser (wavelength = 632.82 nm) and an Olympus 50× objective. The serpentine spectra were acquired for 30 s with an accumulation of 10 cycles in the Raman shift interval of 1200–200 cm^{-1}.

https://doi.org/10.5194/egusphere-2026-3264
Preprint. Discussion started: 16 June 2026

Spectra were fitted using a MATLAB algorithm that corrected the baseline by combining asymmetric least squares (ASL) and a polynomial fit. Peaks were fitted within a local window using a Voigt (pseudo-Voigt) peak detection function.

2.3.2 Scanning Electron microscopy

The starting material and experimental microstructures were imaged with a ZEISS (former LEO) GEMINI 1530 scanning electron microscope (SEM) at BGI, operating at 20 kV and a beam current of 300 pA. Images were collected in back-scattered electron (BSE) mode, which provides sufficient contrast between antigorite and its dehydration products.

Energy-dispersive X-ray (EDS) and electron backscatter diffraction (EBSD) analyses were performed simultaneously using the same SEM, equipped with an X-Max EDS detector and a Nordlys EBSD detector from Oxford Instruments. The operating voltage was 20 kV and a beam current of about 2 nA. Samples were coated with a 5 nm thick carbon layer before analysis to avoid charging effects. Indexing and data treatment were performed with AZTEC software (Oxford Instruments).

Quantitative chemical analyses were performed with a JEOL JXA-8200 electron microprobe at an acceleration voltage of 15 kV. Calibration was carried out using silicates, oxides, and metals. A beam current of 15 nA and a beam diameter of 60 µm were applied to all phases analysed.

2.3.3 Transmission electron microscopy

Thin foils measuring ca. 20 x 10 x 2 µm were cut out across the dehydration vein antigorite interfaces with the help of a focused ion beam instrument (FIB; FEI Scios DualBeam) using a Ga+ ion beam at 30 kV and 3-30 nA. The foils were subsequently thinned to a thickness of 100-300 nm using a low current of 45-100 pA. Energy-dispersive X-ray spectroscopy (EDXS) of the thin foil was performed with a field emission scanning transmission electron microscope (FEI, Titan G2 80-200 S/TEM) equipped with an EDXS system (4 silicon drift detectors, Bruker Quantax). The EDXS chemical maps were taken at a resolution of 12-15 nm per pixel and a dwell time of 16 µsec using a sub-nanometre-sized electron beam with less than 0.02 nA probe current at 200 kV acceleration voltage.

2.3.4 SEM image analysis

Images were collected systematically at different regions of the capsule with the same magnification of 800x. Three images were taken at the top, centre, and bottom of the capsules, positioned between the two lateral edges and along the mid-vertical axis of the capsules.

The SEM images were analysed with a MATLAB algorithm that segments and extracts the pixels associated with dehydration products, which can be distinguished from the initial material by their brighter grey tones, related to their higher Si and Fe contents.

Basic statistical measurements were performed on the segmented images of dehydration products, referred to as “clusters”, which consist of one or more grains of minerals produced by dehydration of antigorite. The measurements include the number of clusters, their area, length and orientation. Clusters smaller than 10 pixels were filtered out before statistical analysis of

https://doi.org/10.5194/egusphere-2026-3264
Preprint. Discussion started: 16 June 2026

cluster area, as well as segments with less than 5 pixels. For shape orientation analysis, the image was skeletonized before measurement using the MATLAB function "bwmorph" (MATLAB, 2010). This processing identified the mid-section of clusters and reduces them to lines, considering a minimum of 8 connected pixels.

Orientation measurements were performed on the skeleton segments with a custom MATLAB function. This function first extracts the (x, y) coordinates of each connected skeleton segment, then applies Principal Component Analysis (PCA) to determine the cluster principal elongation axis, which is then used to determine the cluster orientation. The length of the cluster is then defined by the end points of this best-fit line.

3 Results

Dehydration experiments were conducted under different stress conditions and at pressures and temperatures within the antigorite stability field, leading to distinct microstructural changes and mechanical responses. Under incipient dehydration conditions, the resulting clusters are primarily composed of nanocrystalline olivine, orthopyroxene and relict antigorite. The microstructures of these clusters differ between static and deforming dehydration scenarios. Complete dehydration of antigorite results in the formation of porous aggregates of olivine, orthopyroxene and garnet. The following sections present the main microstructures observed under different experimental conditions.

3.1 Microstructures produced during static antigorite dehydration

Despite the formation of dehydration products and increased porosity, evidence for mechanical failure was not observed during incipient or complete antigorite dehydration. The capsules themselves were not deformed, except for an upward bending of the fully dehydrated sample (Figure 5 a). This bending likely developed during the decompression step. Transgranular fractures with evidence of displacement are not observed in the samples, indicating that static dehydration did not promote deformation or embrittlement of the samples and that the sample column was not disproportionately loaded during compression.

At 560 °C, static dehydration of antigorite for 60 minutes (M910) resulted in the formation of clusters consisting of nano- to micro aggregates of olivine and possibly enstatite, within and at antigorite grain boundaries (figure 3 b-h). The aluminium-rich antigorite areas remained stable at this temperature and pressure; clusters formed around these regions, but not within them (Figure 3 g). Locally, clusters are aligned along antigorite cleavage planes and fractures, however, they do not form veins (figure 3-e) but are aligned on the grain boundaries of the antigorite crystals. These clusters have a median area of 0.47 ± 0.2 µm² (n=2072), reaching a maximum of 14 ± 0.2 µm² (n=2072). The clusters in the experiment M910 have a modal abundance of 1.5% in the whole sample, which corresponds to a porosity of ~1.7% at this stage. Enstatite is observed together with olivine (Figure 3 h); it has a slightly darker grey colour in the backscatter images and a fibrous habit.

The sample annealed for 1260 minutes (M947) at 530 °C and the same pressure shows similar microstructures (Figure 4 a-g) to those of the sample annealed for 60 minutes at higher temperature. The clusters have a median area of 0.51 ± 0.2 µm²

https://doi.org/10.5194/egusphere-2026-3264
Preprint. Discussion started: 16 June 2026

(n=2759) and a maximum area of 32.4 ± 0.2 µm² (n=2759). However, veinlets are observed locally (figure 4 b and d), which were absent in the previous experiment. These veinlets are common at capsule edges and at boundaries of long antigorite grains and they are up to 29.1± 0.5 µm in length. The modal abundance of the clusters in the whole sample is 1.6%, thus, no significant increase in dehydration products is observed, despite the longer annealing time. Growth of olivine surrounding magnetite grains is not observed in these experiments.

At 712 °C, the antigorite core formed a fully dehydrated porous aggregate (Figure 5). Consequently, the porosity of the sample increased to approximately 18%, with the phases present being olivine (~67%), garnet (~10%), pre-existing diopside (~4%), and magnetite (~1%) porphyroblasts (Figure 5 f,g). Enstatite and/or chlorite may be present in the matrix; however, their compositions could not be measured with the electron microprobe due to their small grain size.

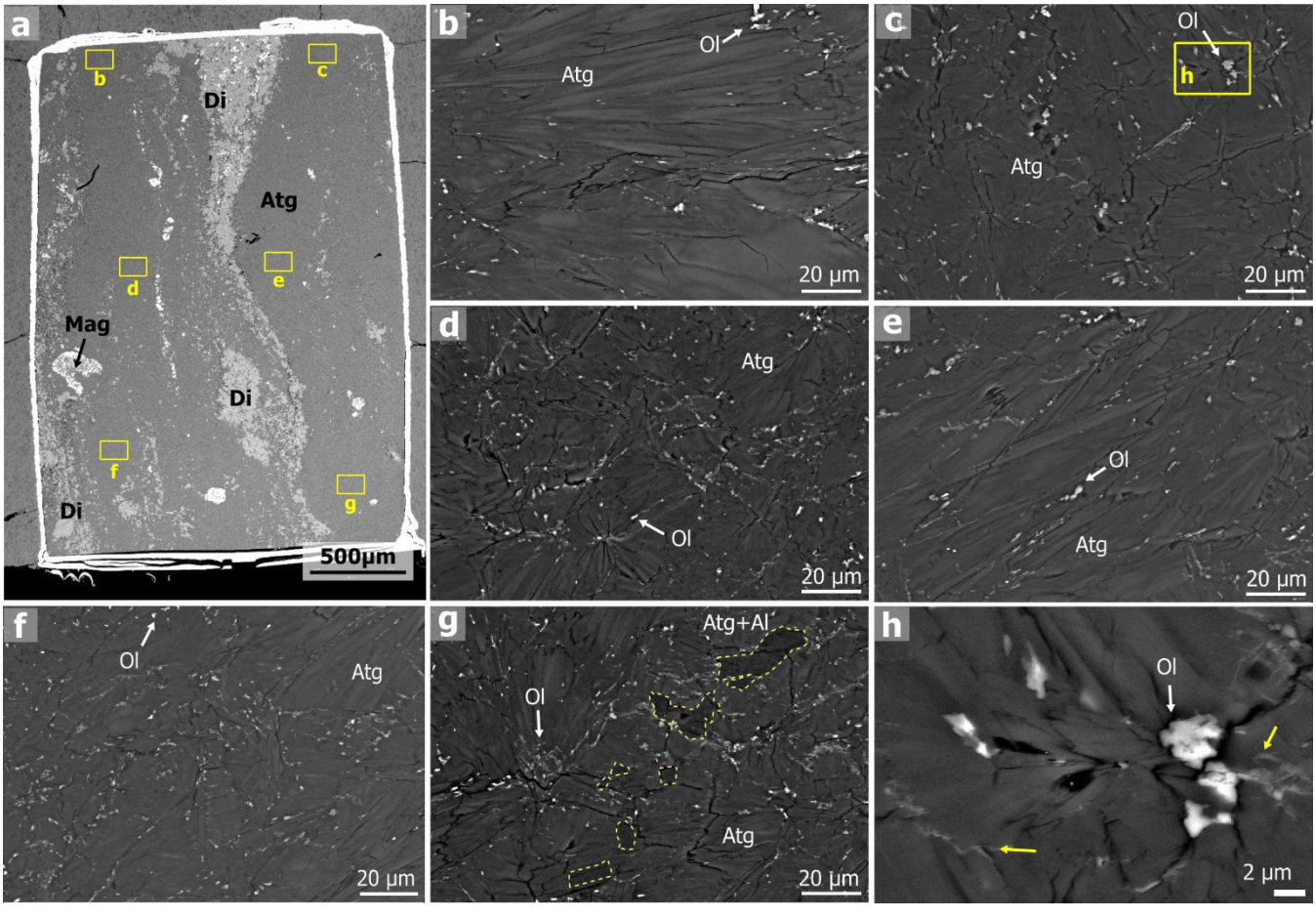

Figure 3 SEM-BSE images of static dehydration of antigorite at incipient conditions (M910 - 3 GPa ; 560°C; 1h). a) Overview of the sample recovered. Yellow squares are the regions show in the insets b-h. Olivine is not visible at this scale. Atg = Antigorite; Di=Diopside; Mag= Magnetite. b-g) Detail of the incipient dehydration microstructure in different regions of the sample. In f the

https://doi.org/10.5194/egusphere-2026-3264
Preprint. Discussion started: 16 June 2026

region marked by yellow polygons are patches where antigorite is richer in aluminium (darker grey tones). Note that olivine is absent inside these areas. h) detail of region in b showing the presence of nano olivine or enstatite.

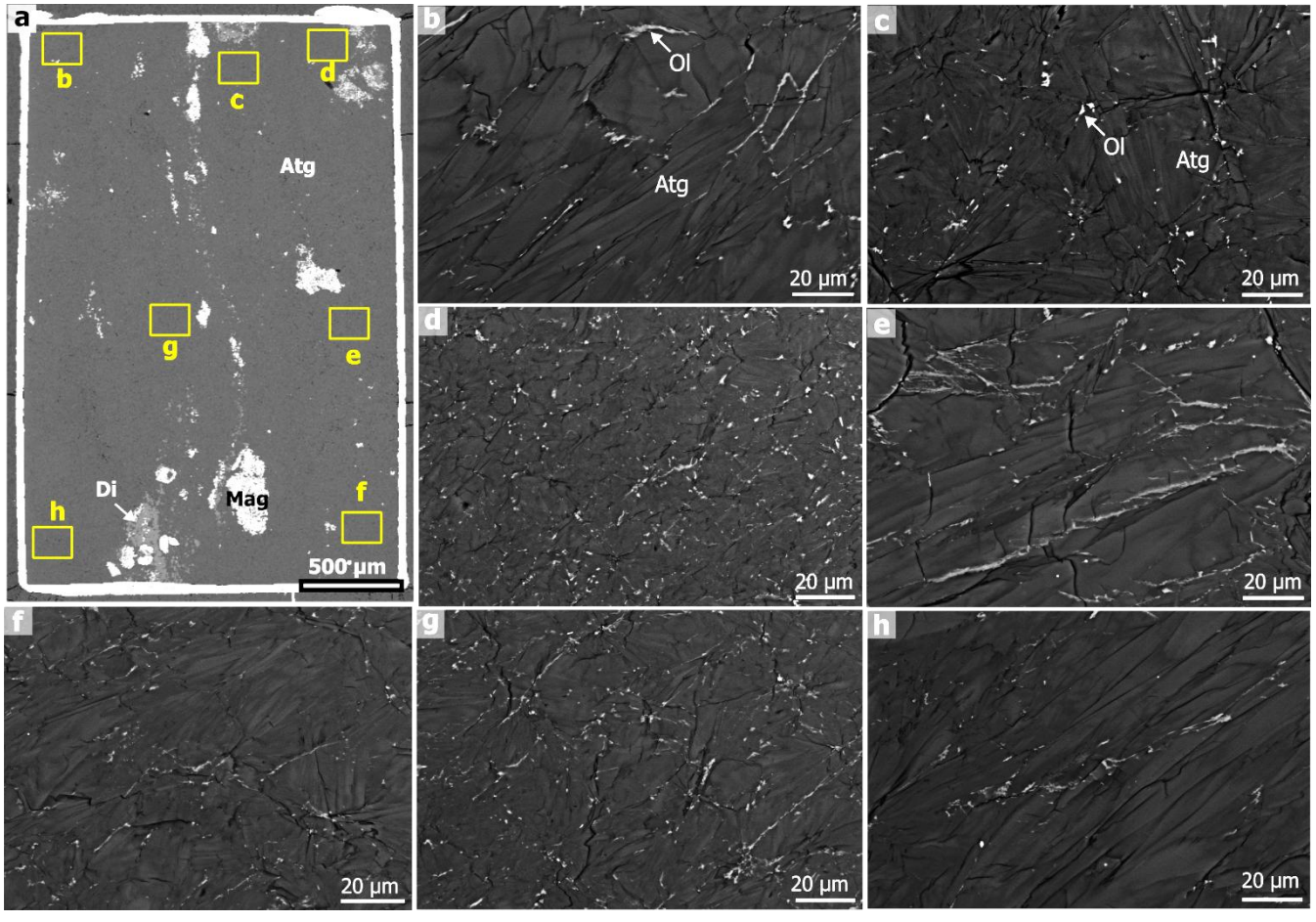

Figure 4: SEM-BSE images of static dehydration of antigorite at incipient conditions (M947 -3 GPa ; 530°C; 21h). Overview of the sample recovered, the yellow squares are the regions in the insets a-g. Olivine is not visible at this scale. Atg = Antigorite; Di=Diopside; Mag= Magnetite. b-g) Detail of the incipient dehydration microstructure in different regions of the sample. A) Detail of olivine veinlet formed at capsule edge. b) Microstructure of clusters of olivine. c) Clusters of olivine where antigorite grains are shorter. d) Olivine veinlets near long antigorite grains.

https://doi.org/10.5194/egusphere-2026-3264
Preprint. Discussion started: 16 June 2026

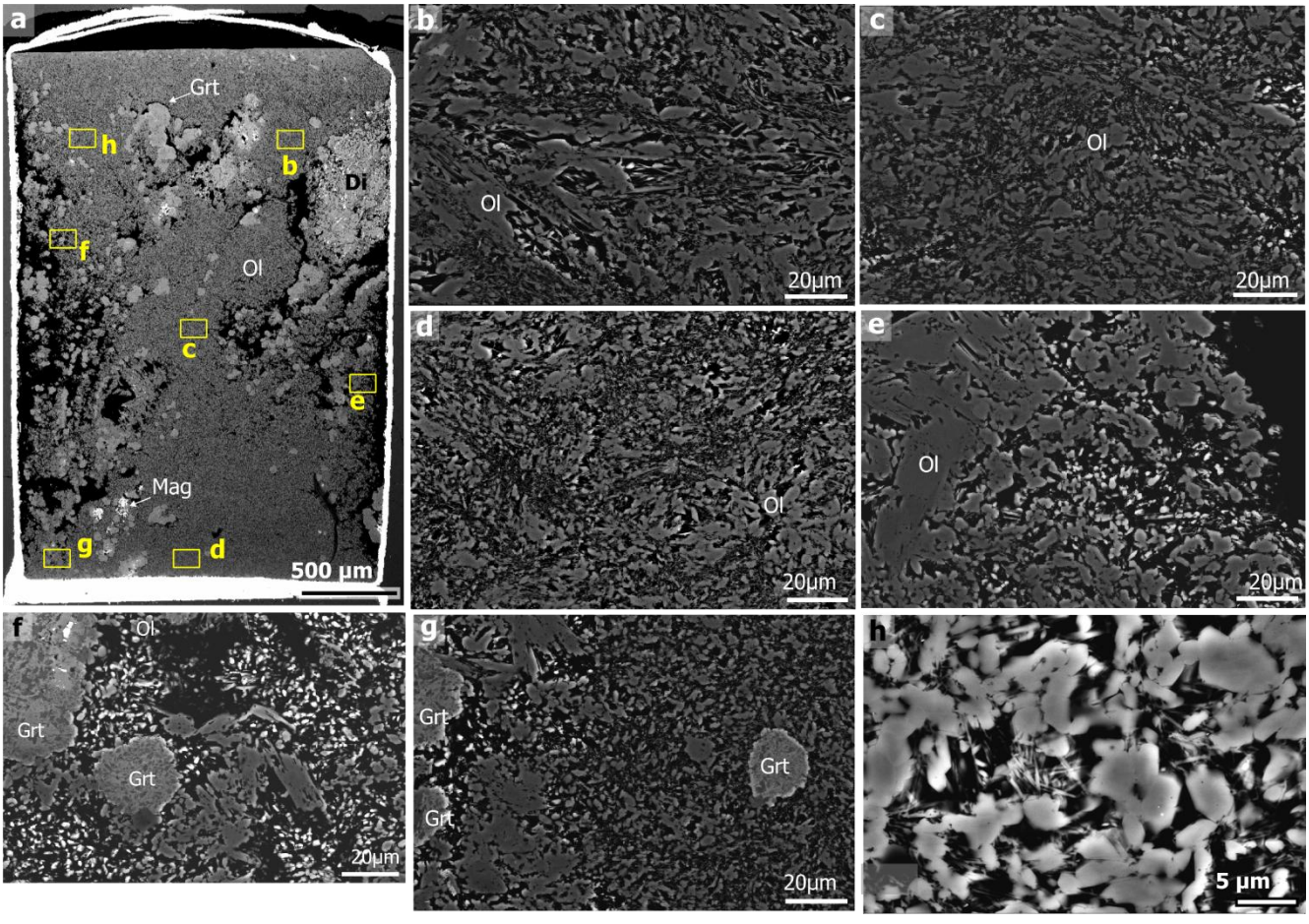

225 **Figure 5 SEM-BSE images of microstructures after complete dehydration of antigorite (M909 – 3 GPa, 712 °C). a) Overview of the sample recovered, Black regions are pore space, dark grey is olivine (Ol), brighter grey is garnet (Grt)/diopside (Di) and white magnetite (Mag). Yellow squares mark regions shown in the insets b-h. b-c) Microstructures of olivine matrix at regions far from sample edges. e-g) Microstructures near sample edges where garnets are abundant. h) Detail microstructure of the olivine matrix showing olivine and needle like crystals.**

230 ### 3.2 Microstructures of long and short duration deformation experiments

In the long duration deformation experiment (M923 - ($\dot{\varepsilon}$) ~ 10^{-5} s^{-1}) under incipient dehydration conditions, the observed capsule strain was 42%, which is 12% more than the apparent strain estimated from the ram displacement. The additional strain may have been applied during compression, since this assembly did not have crushable alumina on both ends. The recovered capsule has bulged (Figure 6 a), resulting in a total sample length decrease of 1.53 ± 0.1 mm in the vertical direction
235 and an increase of 1.00 ± 0.1 mm in the horizontal direction.

Deformation was homogeneous in the antigorite core (Figure 6 a). At the sample's top corners, short shear fractures contain olivine crystals with an apparent rotation microstructure (Figure 6 h). Antigorite crystals are bent near shear fractures and the sample centre. Dehydration clusters evolved into connected vein networks featuring rounded antigorite fragments (Figure 6

https://doi.org/10.5194/egusphere-2026-3264
Preprint. Discussion started: 16 June 2026

d). The median area is 0.65 ± 0.4 µm² (n=4930), and the modal abundance of clusters increased from 1.6% in static dehydration to 17.1%. The occurrence of clusters is much reduced in the top and bottom regions between the sample diagonals (Figure 6 c,f).

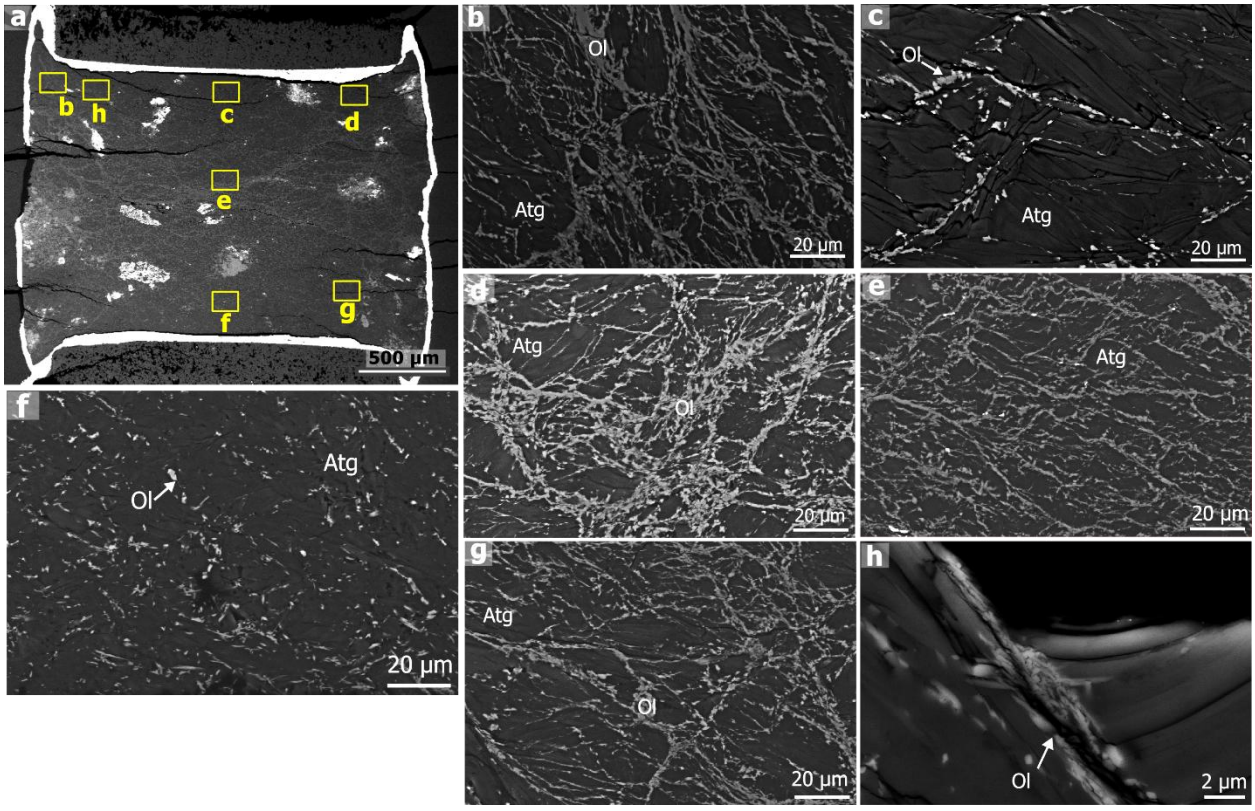

Figure 6 SEM-BSE images of incipient dehydration of antigorite deformed at the slower strain rate (M928 – 3 GPa, 529°C $\dot{\varepsilon} \sim 10^{-5}$ s^{-1}) . a) Overview of the sample. Letters in yellow correspond to locations of images b-h. Atg= antigorite, Ol=olivine.

At incipient dehydration temperatures and short deformation duration (M928 - $\dot{\varepsilon} \sim 10^{-4}$ s^{-1}), the antigorite core showed a strain of 46%, which is 16% more than the apparent strain estimated from the ram displacement. This can again be attributed to deformation during compression. As in the slow strain rate experiment, the capsule bulged horizontally. The total capsule shortening is 1.75 ±0.2 mm, with total increase in the horizontal direction of 0.72 ± 0.1 mm.

A prominent fracture with an angle of 39.9° ± 10° relative to the compression axis extends from the top left to the bottom right of the sample (Figure 7 a), indicating mechanical failure of the sample and possible embrittlement. Secondary fractures are also present in the top right and bottom left regions, though they do not cross the entire sample (figure 7 b,g). Both sets of fractures intersected regions containing dehydration clusters and the orientation of the fractures does not always coincide with the orientation of the clusters (figure 7 b,f).

https://doi.org/10.5194/egusphere-2026-3264
Preprint. Discussion started: 16 June 2026

The microstructure of clusters differs from the static (M910, M947) and long deformation experiment (M923). Clusters are now connected and form veins (Figure 7 c, g) but not connected networks. They concentrate along sample diagonals and the central horizontal axis; between these regions they are scarce or absent, as observed in the slow strain rate experiment (Figure 6 c). The cluster area increased from 0.47 ± 0.2 µm² in the static experiment to a median of 0.76 ± 0.4 µm² (n = 5793).

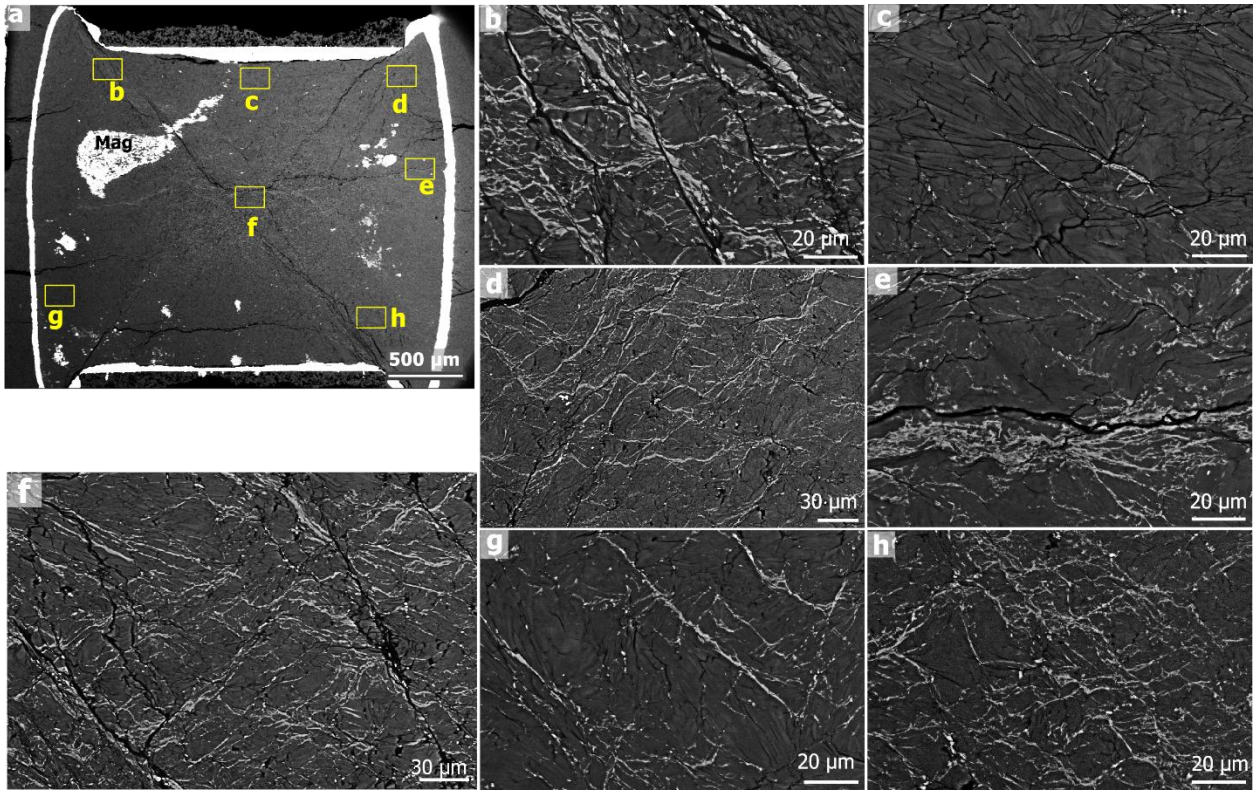

Figure 7- SEM-BSE images of incipient dehydration of antigorite deformed at fast strain rate (M928 -3 GPa ,529°C, $\dot{\varepsilon} \sim 10^{-4}$ s^{-1}). a) Overview of the sample, Mag=magnetite. Letters in yellow correspond to locations of images b-h. Dark grey phase inside the capsule corresponds to antigorite, light grey consists of dehydration clusters.

Detailed TEM analysis of a dehydration vein from this experiment (M928) shows that it consists of a polymineralic aggregate (Figure 8). The phases identified are olivine (59%), orthopyroxene (36%) and relicts of Al-rich antigorite (6%). Grain sizes of these minerals are mostly in the nanometre range and a few relict antigorite grains reached the micron scale (Figure 8).

https://doi.org/10.5194/egusphere-2026-3264
Preprint. Discussion started: 16 June 2026

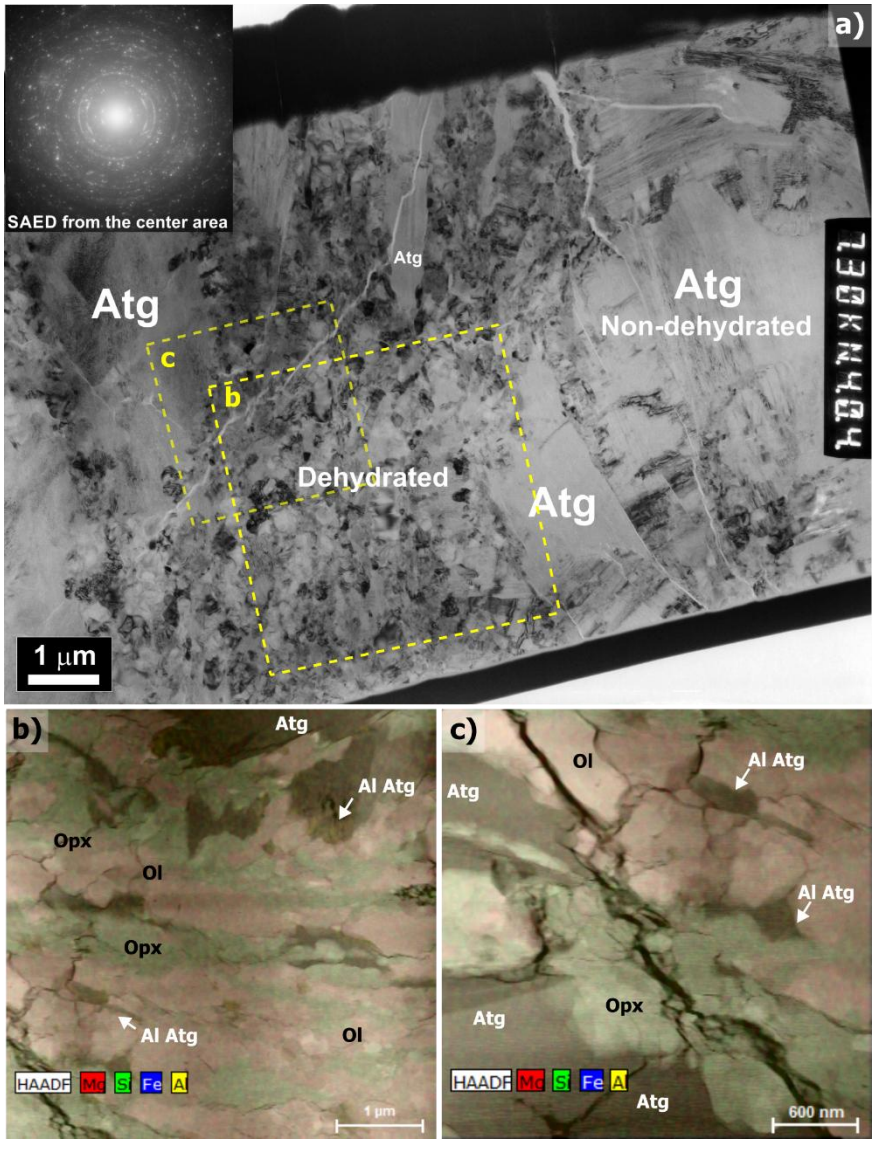

Figure 8 – TEM analysis of a dehydration vein in the experiment M928. A) Bright field TEM image of the dehydrated vein and surrounding antigorite crystals. Selected area diffraction patterns from the center of the dehydrated area, showing the polycrystalline nature of the vein. Yellow insets are regions where EDS maps were performed. b) Large area EDS map of the dehydration vein .c) Smaller area EDS map of same dehydration vein shown in b. Atg=antigorite; Al-Atg = Aluminium rich antigorite; Ol=Olivine; Opx= Orthopyroxene.

3.3 Cluster orientation analysis

Shape orientation of clusters differs between static and deformation experiments. Figure 9 shows the orientations in a polar histogram weighted by cluster length, defined as the distance between the end points of their principal elongation axis. In the

https://doi.org/10.5194/egusphere-2026-3264
Preprint. Discussion started: 16 June 2026

static experiments (Figure 9 a,b), most elongated clusters are oriented at angles between 15-25° relative to the sample horizontal axis. The major difference resulting from the longer static run is an increase in the maximum cluster length, from 8.6 µm to 215.8 µm, within the same angle range. When deformation is applied, the clusters become oriented in the range of 140°-175° (Figure 9 c,d), which corresponds to 50° - 85° relative to the main stress direction. As in the static experiments, the longer run duration results in an increase of the maximum elongation from 25 µm to 58 µm. It can also be observed that the longer deformation experiment (M923) tends to contain more clusters that are parallel to the horizontal axis than in the short deformation experiment (M928).

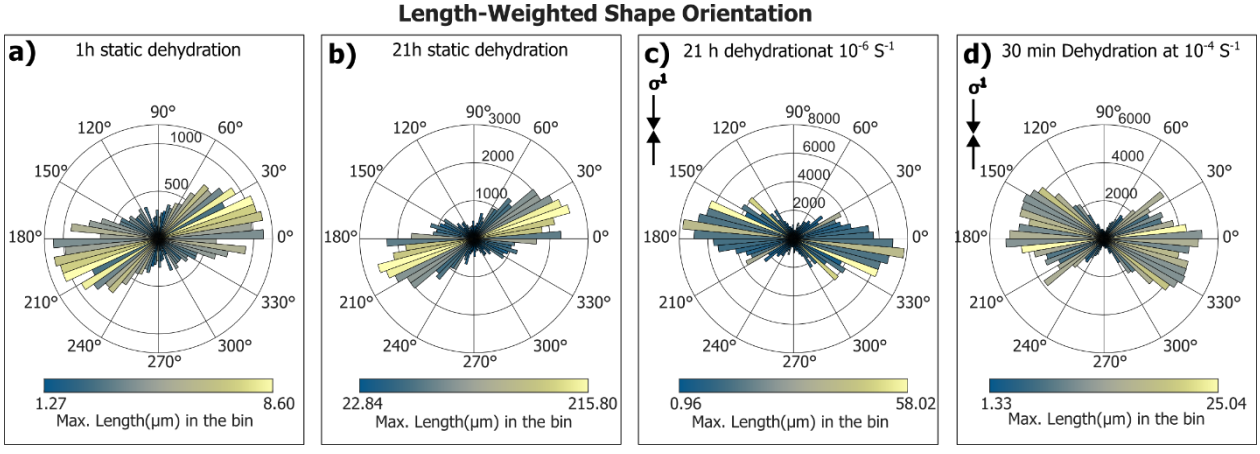

Figure 9 - Length-weighted shape orientation of clusters for the whole capsule in different experiments. The radius corresponds to the sum of the cluster lengths in microns, the colour corresponds to the maximum cluster length the bin, which spreads over 5 °. A) Shape orientation of the static experiment annealed for 1 hour (M910). B) Orientation of clusters produced after annealing for 21 hours (M947). C) Orientation of clusters from long deformation experiment (M923). D) Orientation of clusters in the short deformation experiment (M928). Arrows indicate compression direction in c and d.

3.4 EBSD analysis of dehydration products

EBSD analyses shows evidence of topotactic growth of olivine in experiments after complete dehydration and after long deformation (figure 10). In the starting material, the poles of the basal planes {001} of antigorite show a broad girdle distribution dipping slightly to the NW direction of the pole figure (Figure 10a). {010} poles form a broad maximum in the SE quadrant indicating an axially symmetric CPO pattern around (010). After complete dehydration (M909, Figure 10d) there is some parallelism in the weak CPO of the resulting olivine: the {001} poles form a maximum parallel to {010} of antigorite and the {100} poles have a maximum parallel to {001} of antigorite. After 1 h of static, antigorite and olivine do not show a clear topotactic relationship (Figure 10 b,e).

In the long deformation experiment with incipient dehydration (M923, Figure 10 c,f), basal planes of antigorite form an extended maximum between the compression (Y) and intermediate (Z) direction of the pole figure, combined with a maximum

https://doi.org/10.5194/egusphere-2026-3264
Preprint. Discussion started: 16 June 2026

of {010} in the extension (X) direction (Figure 10 c). In the same sample the olivine CPO is rather weak with concentration of {100} poles along the compression (Y) and intermediate (Z) directions as well as a concentration of {010} poles in the extension direction (X). Even though there is some correspondence between crystallographic directions in the two phases (e.g. antigorite and olivine {100} and {010} respectively) it is not clear if this is caused the transformation or the concurrent deformation.

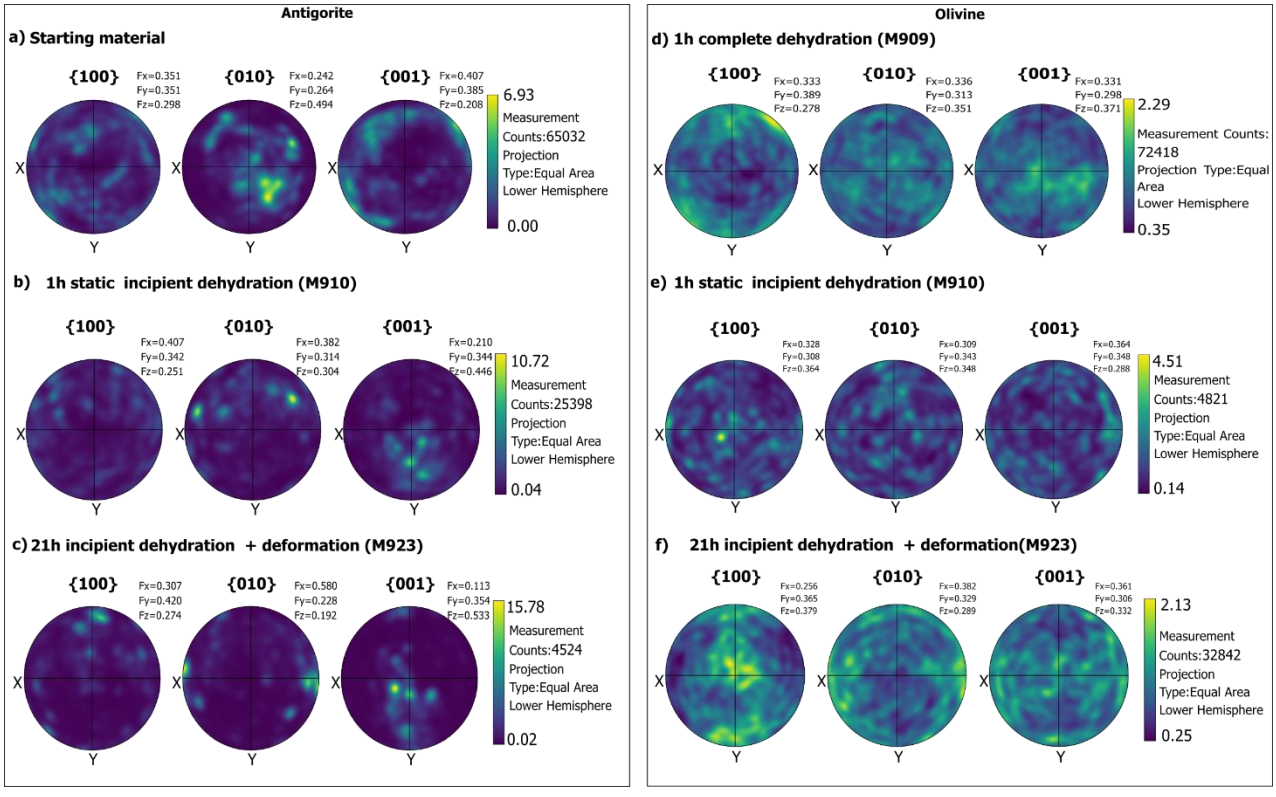

Figure 10 - Pole figures of antigorite and olivine before and after dehydration experiments. X axis correspond to core short axis, Y axis to the core longer axis which is parallel to compression direction in M923 . Equal area projection of the lower hemispheres. a) Pole figures of antigorite in the starting material, grain count = 1328. b) Antigorite pole figure after 1 h of static incipient dehydration(M910), grain count = 611. c) Antigorite pole figure after 21 h deformation under incipient dehydration conditions(M923), grain count = 30. d) Olivine pole figure after complete dehydration(M909), grain count = 2346. e) Olivine pole figure after 1 h static incipient dehydration(M910), grain count = 123. f) Olivine pole figure after 21 h deformation under incipient dehydration conditions(M923), grain count = 975.

4 Discussion

This study is aimed at investigating the deformation behaviour of antigorite under different temperatures and strain rates at pressures relevant to intermediate-depth earthquakes (~3 GPa = ~90–100 km). Specifically, we have examined which conditions might lead to the mechanical failure of serpentine and whether the dehydration products influence deformation

https://doi.org/10.5194/egusphere-2026-3264
Preprint. Discussion started: 16 June 2026

behaviour. Our experimental results indicate that nucleation and microstructural development of dehydration products in antigorite are controlled by its microstructural characteristics, chemical heterogeneity and deformation conditions.

Under static conditions, dehydration proceeds through dispersed olivine nucleation on grain boundaries at incipient dehydration temperatures, whereas complete dehydration leads to increased porosity at higher temperatures. In contrast, deformation imposes a first-order control on the localization of the dehydration reaction and the formation of olivine veins and networks. In this section, we discuss these results in the context of previous studies on antigorite dehydration, as well as their implications and current limitations.

4.1 Antigorite dehydration in static experiments at 530-560°C and 3 GPa

Incipient antigorite dehydration at temperatures below the nominal stability field has been reported in both experimental and field-based studies, indicating that the breakdown of antigorite begins progressively at temperatures significantly below the bulk reaction to form olivine + enstatite + H_2O (Eberhard et al., 2025; Huber et al., 2024; Merkulova et al., 2016). The presence of dehydration products at <600 °C in our experiments may therefore reflect the early stage of this distributed breakdown.

Proposed mechanisms for this early olivine formation primarily invoke local chemical heterogeneities either within the serpentine mineral itself or due to coexisting phases. One possibility is the reaction brucite + antigorite = olivine + water and another involves redox reactions with magnetite (Eberhard et al., 2025; Merkulova et al., 2016). Neither mechanism is consistent with our observations. In the first case, no brucite was detected in the starting material plus the clusters generally contain orthopyroxene. In the second case, clusters do not form preferentially adjacent to magnetite grains and no reaction rims are observed.

Heterogeneities in FeO, SiO_2 and Al_2O_3, have also been proposed to influence the dehydration temperature of serpentinites. (Huber et al., 2024) demonstrated that regions of serpentine with higher FeO contents dehydrate at lower temperatures and increased SiO_2 levels control the extent of the brucite-out reaction. In contrast, higher Al_2O_3 levels shift the antigorite-out reaction to higher temperatures(Bromiley and Pawley, 2003). However, our starting material does not contain significant heterogeneities in either Fe or Si content, at least not at the fine scale that would implicate them in cluster formation. The aluminium heterogeneity in the samples is also unlikely to be relevant to the low temperature incipient dehydration, although it does explain the formation of garnet regions after complete dehydration.

A final possibility is that other volatile components (e.g., C-, S-, or Cl-bearing species) reduce the effective activity of H_2O, thereby broadening the temperature interval over which serpentine destabilizes. While speculative, this mechanism is thermodynamically plausible and would require only trace concentrations of additional volatiles.

The lack of fractures and displaced faults, which would be indicative of dehydration embrittlement, in the static dehydration experiments indicates that dehydration alone does not trigger brittle failure. Although fast fluid escape is expected during complete dehydration, fluid pressure under our experimental conditions was insufficient to produce embrittlement. In both incipient and complete dehydration scenarios, the resulting material appears mechanically weaker than the starting material due to grain size and modal contrasts between olivine and antigorite, as well as the increased porosity. This weakening

https://doi.org/10.5194/egusphere-2026-3264
Preprint. Discussion started: 16 June 2026

represents a mechanical preconditioning of the aggregate rather than failure itself. Thus, subsequent changes in pressure, temperature and deviatoric stress may promote failure in a material that has already been weakened by dehydration.

Preferential shape orientation of clusters during incipient static dehydration may indicate that antigorite anisotropy plays a role in the nucleation of olivine. Antigorite in the starting material shows an interlocking microstructure with radial growth, as indicated by the dispersion of basal planes in the pole figure (Figure 10 a), with crystal elongation parallel to the a<100> and b<010> directions. Although weak, the basal planes of antigorite display a CPO oriented at ± 40° from the longer core axis. The apparent preferential shape orientation may reflect topotactic growth of olivine a(100) or b(010) parallel to antigorite c(001) planes.

The images used for determination of cluster shape orientation show elongated crystals in which antigorite elongation-cleavage planes are oriented at an angle similar to the cluster shape orientation (~15-25°). Such shape orientation relationships are not observed when antigorite grains are not elongated, and cluster orientations appear more random (Figure 11). Previous studies have shown that olivine can share a topotactic relationship when precipitating from antigorite in natural and experimental conditions (Padrón-Navarta et al., 2015), where olivine a or b planes grow parallel to the basal planes (001) of antigorite. In summary, these results show that incipient dehydration occurs at temperatures within the antigorite stability field. Although the causal by process is unclear, it does not appear to require deformation to initiate. The incipient reaction is spatially distributed, anisotropy-controlled, and most likely mechanically weakening, but insufficient on its own to produce embrittlement.

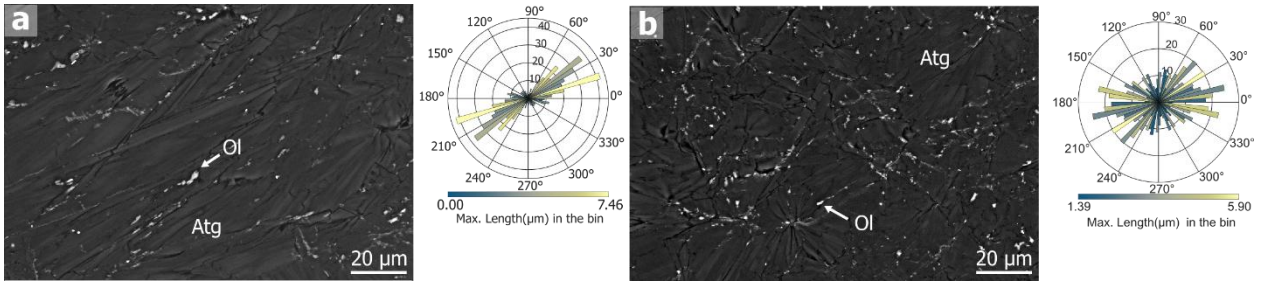

Figure 11- Individual images of sample M910 and its corresponding cluster shape orientation. A) Sample region in the center of the capsule where atigorite grains are elongated. b) Sample region in the center of the capsule where antigorite grains are not elongated.

4.2 Modulation number in antigorite

Changes in the polysome type of antigorite might offer an explanation for continuous incipient dehydration with increasing pressure and temperature (Wunder et al., 2001). However, single crystal X-diffraction(XRD) of the starting material shows it to have the length of the a unit cell with a-axis is 38.304(17) Å, corresponding to a polysome of m = 15 (Capitani and Mellini, 2007). HR-TEM of a vein from the short deformation experiment (M928) also showed a modulation m = 15 for one antigorite crystal analysed (Figure S4). Thus, the localized incipient dehydration observed in our experiments is unlikely to be due to changes in polysome type.

https://doi.org/10.5194/egusphere-2026-3264
Preprint. Discussion started: 16 June 2026

4.3 Incipient dehydration under deviatoric stress

The microstructures produced in our deformation experiments at 3 GPa and ~530 °C are consistent with previous studies performed at confining pressures of 1-1.5 GPa (Eberhard et al., 2025; French et al., 2019). Although clusters are found in static experiments, in fast and slow deformation experiments these clusters present distinct microstructures. They are bigger, more abundant and with higher connectivity than in static experiments. Additionally, they are localized in the more deformed regions of the sample.

Our experiments indicate that deviatoric stress influences the development of antigorite dehydration at different strain-rate conditions. Increased localized dehydration is unlikely to be related to chemical or mineralogical heterogeneities, since the shape-preferred orientation of veins correlates with the orientation of high strain domains. Deformation likely enhances porosity connectivity and promotes formation of veins instead of dispersed clusters. The contrast in grain size between new olivine grains (<2 μm) and antigorite (>20 μm) may promote strain localization, resulting in brittle failure at fast strain-rate and homogeneous deformation at slower strain-rate.

Localized incipient dehydration of antigorite within its nominal stability field during deformation has been attributed to enhanced reaction kinetics due to plastic deformation (Eberhard et al., 2025), local increase in temperature due to shear heating and local increase in fluid pressure (French et al., 2019). An increase in dislocation density or decrease in grain size due to grain comminution can influence thermodynamic stability of antigorite by lowering the activation energy necessary for dehydration (Eberhard et al., 2025; French et al., 2019). However, in our fast strain rate experiments, dehydration veins form with small grain sizes that, with time, anneal without significant grain comminution of antigorite, which occurs during the brittle fracturing stage.

The localization of dehydration clusters may also reflect the topotactic relationship between olivine and antigorite, combined with anisotropy in antigorite strength and permeability (Kawano et al., 2011; Shao et al., 2025). Experimental results show that antigorite has strong mechanical anisotropy, with the highest strength for loading normal to the foliation (approximately parallel to the c-axis) and a pressure-dependent change in anisotropy within the foliation plane: at low pressure, the a-axis corresponds to the hard-friction direction, whereas at higher pressure, the b-axis becomes the hard-slip direction (Shao et al., 2025). These authors also observe dehydration products formed during deformation, although they do not attribute dehydration to the relationship between the hard friction axis and stress field. Our experiments seem to indicate that dehydration bands preferentially develop along mechanically strong orientations, where stress concentrations are greatest. Alignment of basal planes perpendicular to the principal stress may therefore promote precipitation of dehydration products and explain the sub horizontal orientation of veins in deformed samples.

Newly formed olivine grains are much smaller than antigorite (Figure 7b) and have higher density, which could create potential regions of strain localization. Pore space generated during this stage provides pathways for fluid migration, which may locally increase fluid pressure. The volume fraction of the weaker phase in an aggregate strongly influences deformation style (Ferrand

https://doi.org/10.5194/egusphere-2026-3264
Preprint. Discussion started: 16 June 2026

et al., 2017; Hilairet et al., 2024). These studies show that small amounts of antigorite (5 vol%.) lead to hardening of olivine-antigorite mixtures, whereas higher antigorite fractions weaken the aggregate and concentrate strain in the weaker phase. In our fast strain-rate experiment, newly formed olivine veins may behave as mechanically weak zones due to fine grain size and fluid presence, promoting strain localization and brittle fracture. At slower strain rates, interconnected olivine vein networks may accommodate deformation through grain-boundary rotation and dislocation creep at ~530°C, while residual antigorite deforms plastically, resulting in more homogeneous bulk deformation.

One could speculate that if deformation proceeds at slow strain rates, dehydration is enhanced by ductile deformation of residual antigorite, forming more olivine and fluid, which could reverse the phases that control deformation behaviour (Hilairet et al., 2024). The new fluid-rich peridotite could undergo brittle failure due to reduced strength in the presence of trapped fluids, or strain hardening due to the decreased amount of antigorite.

4.4 Implications for intermediate seismicity/subduction zones

Antigorite dehydration is commonly invoked to explain intermediate depth seismicity in subduction zones (Houston, 2015). Numerous studies show that increases in pressure, temperature and deviatoric stress enhance antigorite dehydration, while chemical heterogeneities promote reaction over a range of temperatures (Eberhard et al., 2025; Huber et al., 2022; Padrón-Navarta et al., 2010; Plümper et al., 2017; Schmalholz et al., 2023). Our experiments demonstrate that, although initial olivine nucleation may occur passively in heterogeneous serpentinite, the formation of interconnected veins requires dynamic deformation.

Dehydration embrittlement is one of the mechanisms proposed to be responsible for intermediate-depth earthquakes; however detailed microstructural evidence remains lacking. At strain rates applicable to subduction zones, antigorite and olivine may deform in the plastic regime. However, serpentine is unlikely to occur as a continuous layer in the subducting slab; instead it probably forms mechanically weaker patches embedded in a stronger peridotite matrix dominated by olivine. Thus, serpentine is the weaker phase in the subduction slab. Experimental and natural observations indicate that serpentine dehydration proceeds in multiple stages (Eberhard et al., 2025; Huber et al., 2022; Muñoz-Montecinos et al., 2024; Plümper et al., 2017), releasing fluid and generating olivine veins that may evolve toward reduced permeability and strain hardening. As these patches progress through successive dehydration stages under increasing pressure and temperature, the resulting composite material may ultimately approach mechanical instability.

We therefore suggest that intermediate-depth seismicity may reflect a continuum of dehydration-assisted mechanical processes rather than a single embrittlement event. Early fluid-release stages could contribute to episodic tremor, whereas larger earthquakes may occur when weakened serpentinite domains reach critical stress conditions near the limits of antigorite stability.

https://doi.org/10.5194/egusphere-2026-3264
Preprint. Discussion started: 16 June 2026

5 Conclusions

Localized dehydration of antigorite within its stability field can initiate under hydrostatic conditions but is markedly enhanced by deformation. Although dehydration alone is insufficient to cause embrittlement under typical conditions, stress-enhanced dehydration, evolving microstructures, and fluid production progressively modify the mechanical behaviour of serpentinite. As residual antigorite dehydrates and fluid-rich peridotite develops, deformation mechanisms may shift, potentially leading to brittle instability. Intermediate-depth earthquakes are therefore more likely to reflect a continuum of dehydration-assisted mechanical processes rather than a single classical dehydration embrittlement event. Future experiments with acoustic emission monitoring may elucidate whether localized incipient dehydration has seismogenic potential and clarify the failure observed at faster strain rates.

6 Code and data availability

Images, chemical and structural data as well as codes used for the elaboration of the figures in this manuscript are available at Zenodo repository with restricted access to be granted to reviewers during the review process.

7 Team list

Danielle Silva Souza, Bayerisches Geoinstitute
Daniel Frost, Bayerisches Geoinstitute
Florian Heibalch, Bayerisches Geoinstitute
Marcel Thielmann, Institute of Earth Sciences, University of Bonn

8 Author contributions

D.S. designed and conducted the experiments, analyzed the data, and wrote the original manuscript. D.F. and F.H. contributed to the experimental design and manuscript review. M.T. developed the image segmentation and data analysis software, contributed to data analysis, and was responsible for project administration and funding.

9 Competing interests

The authors declare that they have no conflict of interest.

https://doi.org/10.5194/egusphere-2026-3264
Preprint. Discussion started: 16 June 2026

10 Acknowledgements

The authors thank Tiziana Boffa Ballaran and Nobuyoshi Miyajima, for assistance with X-Ray diffraction and TEM analyses, as well as Raphael Njul, Erik Konrad and Dorothea Wiesner for the sample preparation of recovered samples. This work was supported by Emmy-Noether program of the German Research Foundation (DFG).

11 References

Bromiley, G. D. and Pawley, A. R.: The stability of antigorite in the systems MgO-SiO_2 -H_2 O (MSH) and MgO-Al_2 O_3 -SiO_2 -H_2 O (MASH): The effects of Al^{3+} substitution on high-pressure stability, American Mineralogist, 88, 99–108, https://doi.org/10.2138/am-2003-0113, 2003.

Capitani, G. C. and Mellini, M.: High-resolution transmission electron microscopy (HRTEM) investigation of antigorite polysomes (m = 15 to 18), American Mineralogist, 92, 64–71, https://doi.org/10.2138/am.2007.2188, 2007.

Chollet, M., Daniel, I., Koga, K. T., Morard, G., and Van De Moortèle, B.: Kinetics and mechanism of antigorite dehydration: Implications for subduction zone seismicity, J. Geophys. Res., 116, B04203, https://doi.org/10.1029/2010JB007739, 2011.

Dobson, D. P., Meredith, P. G., and Boon, S. A.: Simulation of Subduction Zone Seismicity by Dehydration of Serpentine, Science, 298, 1407–1410, https://doi.org/10.1126/science.1075390, 2002.

Eberhard, L., Mazzucchelli, M. L., Schmalholz, S. M., Stünitz, H., Addad, A., Cordier, P., and Plümper, O.: Coupling antigorite deformation and dehydration in high-pressure experiments, Contrib Mineral Petrol, 180, 64, https://doi.org/10.1007/s00410-025-02255-z, 2025.

Ferrand, T. P., Hilairet, N., Incel, S., Deldicque, D., Labrousse, L., Gasc, J., Renner, J., Wang, Y., Green Ii, H. W., and Schubnel, A.: Dehydration-driven stress transfer triggers intermediate-depth earthquakes, Nat Commun, 8, 15247, https://doi.org/10.1038/ncomms15247, 2017.

French, M. E., Hirth, G., and Okazaki, K.: Fracture-induced pore fluid pressure weakening and dehydration of serpentinite, Tectonophysics, 767, 228168, https://doi.org/10.1016/j.tecto.2019.228168, 2019.

Frohlich, C.: Deep earthquakes, Nachdr., Cambridge University Press, Cambridge, 573 pp., 2009.

Gasc, J., Schubnel, A., Brunet, F., Guillon, S., Mueller, H.-J., and Lathe, C.: Simultaneous acoustic emissions monitoring and synchrotron X-ray diffraction at high pressure and temperature: Calibration and application to serpentinite dehydration, PHYSICS OF THE EARTH AND PLANETARY INTERIORS, 189, 121–133, https://doi.org/10.1016/j.pepi.2011.08.003, 2011.

Gasc, J., Hilairet, N., Yu, T., Ferrand, T., Schubnel, A., and Wang, Y.: Faulting of natural serpentinite: Implications for intermediate-depth seismicity, Earth and Planetary Science Letters, 474, 138–147, https://doi.org/10.1016/j.epsl.2017.06.016, 2017.

Hilairet, N., Guignard, J., Ferrand, T. P., Merkel, S., Raterron, P., Ildefonse, B., Fadel, A., and Crichton, W.: Stress Balance in Synthetic Serpentinized Peridotites Deformed at Subduction Zone Pressures, JGR Solid Earth, 129, e2023JB028073, https://doi.org/10.1029/2023JB028073, 2024.

https://doi.org/10.5194/egusphere-2026-3264
Preprint. Discussion started: 16 June 2026

Houston, H.: 4.13 - Deep Earthquakes, in: Treatise on Geophysics (Second Edition), edited by: Schubert, G., Elsevier, Oxford, 329–354, https://doi.org/10.1016/B978-0-444-53802-4.00079-8, 2015.

Huber, K., Vrijmoed, J. C., and John, T.: Formation of Olivine Veins by Reactive Fluid Flow in a Dehydrating Serpentinite, Geochem Geophys Geosyst, 23, e2021GC010267, https://doi.org/10.1029/2021GC010267, 2022.

Huber, K., John, T., Vrijmoed, J. C., Pleuger, J., and Zhong, X.: Pulsed fluid release from subducting slabs caused by a scale-invariant dehydration process, Earth and Planetary Science Letters, 644, 118924, https://doi.org/10.1016/j.epsl.2024.118924, 2024.

Jung, H., Green Ii, H. W., and Dobrzhinetskaya, L. F.: Intermediate-depth earthquake faulting by dehydration embrittlement with negative volume change, Nature, 428, 545–549, https://doi.org/10.1038/nature02412, 2004.

Kawano, S., Katayama, I., and Okazaki, K.: Permeability anisotropy of serpentinite and fluid pathways in a subduction zone, Geology, 39, 939–942, https://doi.org/10.1130/G32173.1, 2011.

Manthilake, M. A. G. M., Walte, N., and Frost, D. J.: A new multi-anvil press employing six independently acting 8 MN hydraulic rams, High Pressure Research, 1–13, https://doi.org/10.1080/08957959.2012.680450, 2012.

Merkulova, M., Muñoz, M., Vidal, O., and Brunet, F.: Role of iron content on serpentinite dehydration depth in subduction zones: Experiments and thermodynamic modeling, Lithos, 264, 441–452, https://doi.org/10.1016/j.lithos.2016.09.007, 2016.

Muñoz-Montecinos, J., Angiboust, S., Minnaert, C., Ceccato, A., Morales, L., Gasc, J., and Behr, W.: Fluid-Driven Shear Instabilities in the Subducted Oceanic Mantle at Intermediate Depths: Insights From Western Alps Meta-Ophiolites, Geochem Geophys Geosyst, 25, e2024GC011581, https://doi.org/10.1029/2024GC011581, 2024.

Okazaki, K. and Hirth, G.: Dehydration of lawsonite could directly trigger earthquakes in subducting oceanic crust, Nature, 530, 81–84, https://doi.org/10.1038/nature16501, 2016.

Padrón-Navarta, J. A., Hermann, J., Garrido, C. J., López Sánchez-Vizcaíno, V., and Gómez-Pugnaire, M. T.: An experimental investigation of antigorite dehydration in natural silica-enriched serpentinite, Contrib Mineral Petrol, 159, 25–42, https://doi.org/10.1007/s00410-009-0414-5, 2010.

Padrón-Navarta, J. A., Tommasi, A., Garrido, C. J., and Mainprice, D.: On topotaxy and compaction during antigorite and chlorite dehydration: an experimental and natural study, Contrib Mineral Petrol, 169, 35, https://doi.org/10.1007/s00410-015-1129-4, 2015.

Plümper, O., John, T., Podladchikov, Y. Y., Vrijmoed, J. C., and Scambelluri, M.: Fluid escape from subduction zones controlled by channel-forming reactive porosity, Nature Geosci, 10, 150–156, https://doi.org/10.1038/ngeo2865, 2017.

Poli, S. and Schmidt, M. W.: Petrology of Subducted Slabs, Annu. Rev. Earth Planet. Sci., 30, 207–235, https://doi.org/10.1146/annurev.earth.30.091201.140550, 2002.

Proctor, B., B. Proctor, and Hirth, G.: Role of pore fluid pressure on transient strength changes and fabric development during serpentine dehydration at mantle conditions: Implications for subduction-zone seismicity, Earth and Planetary Science Letters, 421, 1–12, https://doi.org/10.1016/j.epsl.2015.03.040, 2015.

Raleigh, C. B. and Paterson, M. S.: Experimental deformation of serpentinite and its tectonic implications, J. Geophys. Res., 70, 3965–3985, https://doi.org/10.1029/JZ070i016p03965, 1965.

https://doi.org/10.5194/egusphere-2026-3264
Preprint. Discussion started: 16 June 2026

Schmalholz, S. M., Moulas, E., Räss, L., and Müntener, O.: Serpentinite Dehydration and Olivine Vein Formation During Ductile Shearing: Insights From 2D Numerical Modeling on Porosity Generation, Density Variations, and Transient Weakening, JGR Solid Earth, 128, e2023JB026985, https://doi.org/10.1029/2023JB026985, 2023.

Shao, T., Song, M., Li, J., and Jiang, Z.: Pressure-Induced Change in Mechanical Anisotropy Within the Foliation Plane of Antigorite as an Indicator of the Brittle–Ductile Transition, JGR Solid Earth, 130, e2025JB031143, https://doi.org/10.1029/2025JB031143, 2025.

Wunder, B., Wirth, R., and Gottschalk, M.: Antigorite: Pressure and temperature dependence of polysomatism and water content, ejm, 13, 485–495, https://doi.org/10.1127/0935-1221/2001/0013-0485, 2001.

Zhan, Z.: Mechanisms and Implications of Deep Earthquakes, Annu. Rev. Earth Planet. Sci., 48, 147–174, https://doi.org/10.1146/annurev-earth-053018-060314, 2020.